Clay Minerals, (2016) **51**, 603–613

High-angle annular dark field scanning transmission electron microscopic (HAADF-STEM) study of Fe-rich 7 Å–14 Å interstratified minerals from a hydrothermal deposit

SAYAKO INOUÉ[†,*] AND TOSHIHIRO KOGURE

Department of Earth and Planetary Science, Graduate School of Science, The University of Tokyo, 7-3-1 Hongo, Bunkyo-ku, Tokyo 113-0033, Japan

(*Received 18 November 2016; revised 5 April 2016; Associate Editor: Daniel Beaufort*)

ABSTRACT: The distribution of octahedral cations in the two component layers of a 7 Å–14 Å interstratified mineral with a bulk chemical composition $(Fe^{2+}_{4.12}Mg_{0.07}Mn_{0.01}Al_{1.69}\square_{0.11})(Si_{2.56}Al_{1.44})O_{10}(OH)_8$ was investigated using high-angle annular dark field scanning transmission electron microscopy (HAADF-STEM) in combination with the image simulations. In the 14 Å component layers, comparison between the observed and simulated images revealed that the M4 sites of the interlayer sheets were occupied preferentially by Al together with a small amount of Fe; the other M1, M2 and M3 sites were occupied by dominant Fe and residual Al in equal proportions. Two types of octahedral sheets with disordered and ordered cation distributions were recognized in the 7 Å component layers. The two types of sheets were similar to the octahedral sheet of the 2:1 layer and the interlayer sheet in the 14 Å layer above, respectively. Irregular vertical stacking and lateral contact of the different component layers in structure and chemistry characterized the interstratification, which may be caused by rapid precipitation and accretion of the component layers in hydrothermal environments.

KEYWORDS: HAADF-STEM, interstratified minerals, Fe-rich chlorite, berthierine, octahedral cation distribution.

Chlorite, berthierine and their interstratified minerals are common phyllosilicate minerals that occur in a wide range of geological environments including diagenesis, low- to medium-grade metamorphism and hydrothermal alteration. The crystal structure and cation distribution in clinochlore (a Mg-endmember of chlorite) have been refined using X-ray diffraction (XRD) and spectroscopic techniques (Rule & Bailey, 1987; Bailey, 1988a; Zheng & Bailey, 1989; Welch *et al.*, 1995). Chlorite has a 14 Å unit structure consisting of alternation of the 2:1 layer (TOT) of $\{M1(M2)_2(T)_4O_{10}(OH)_2\}$ and the interlayer sheet or the hydroxide sheet (B sheet) of $\{(M3)_2M4(OH)_6\}$, where M1, M2, M3 and M4 are the octahedral sites occupied by cations such as Fe^{2+}, Mg, Al, Fe^{3+} and so on, and T are the tetrahedral sites usually occupied by Si and Al. Trivalent Al and Fe^{3+} preferentially occupy the M4 sites in the B sheet of clinochlore (*e.g.* Rule & Bailey, 1987; Bailey, 1988a; Zheng & Bailey, 1989; Welch *et al.*, 1995). The structural formulae of 7 Å serpentine group minerals are expressed by a half of chlorite, $(M)_3(T)_2O_5(OH)_4$, in which the distribution

*E-mail: inouesayako@gmail.com
[†]This work was originally presented during the session 'The many faces of chlorite', part of the Euroclay 2015 conference held in July 2015 in Edinburgh, UK.

DOI: 10.1180/claymin.2016.051.4.05

of cations in T and M sites is generally known to be disordered in the Mg-endmembers (*e.g.* Wicks & O'Hanley, 1988; Bailey, 1988b). In contrast, the structure of Fe-rich chlorite, especially the cation distribution in the octahedral sites, has been poorly understood because of its fine grain size and frequent stacking disorder. A similar situation is recognized in Fe-rich serpentine-group minerals such as berthierine and odinite. Furthermore, interlayering of the two minerals occurs frequently (Ahn & Peacor, 1985; Jiang *et al.*, 1992; Slack *et al.*, 1992; Hillier, 1994; Xu & Veblen, 1996), which makes it more difficult to obtain information about the details of crystal structure by convenient techniques.

High-resolution transmission electron microscopy (HRTEM) has contributed significantly to overcome such a difficulty. In particular, a recent imaging technique, referred to as high-angle annular dark field (HAADF) in a scanning transmission electron microscope (STEM), offers the ability to obtain information on the detailed distribution of cations in silicate minerals such as phyllosilicates (*e.g.* Kogure & Drits, 2010) and pyroxenes (*e.g.* Kogure & Okunishi, 2010; Xu *et al.*, 2014), because the contrast in HAADF-STEM images is roughly proportional to the square of average atomic number (Z) (Pennycook & Jesson, 1992). Local composition and occupancy of individual sites can be obtained from measured contrast intensities (Xu *et al.*, 2014). In this study, Fe-rich interstratified minerals of 14 Å chlorite and 7 Å berthierine, which were collected from a hydrothermal vein-type ore deposit, have been investigated by a combination of HAADF-STEM observations and the image simulations to elucidate the distribution of cations in the octahedral sheets in the component layers and the characteristics of their vertical and lateral contacts in the interstratified structure.

SAMPLES AND METHODS

Samples

The sample studied was collected from the Ashio deposit, Tochigi, Japan which is a hydrothermal vein-type ore deposit (Shikazono, 2003). The interstratified mineral of interest occurred as a gangue mineral in mineralized quartz veins. The chemical composition was determined by energy-dispersive X-ray spectrometry (EDS) in scanning electron microscopy (SEM) using thin sections of quartz veins containing the minerals. The chemical formula obtained was expressed as $(Fe^{2+}_{4.12}Mg_{0.07}Mn_{0.01}Al_{1.69}\square_{0.11})(Si_{2.56}Al_{1.44})O_{10}(OH)_8$, on average, assuming that total iron was ferrous and the number of oxygen atoms was 14, and where □ denotes the vacancy. The formation temperature was estimated to be 321°C based on the chlorite geothermometer of Bourdelle *et al.* (2013). The value was consistent with the homogenization temperatures of fluid inclusions in quartz (Shikazono, 2003). For more detailed descriptions of the geological setting and mineralogical characteristics involving chemical compositions, XRD, TEM and the formation temperatures, the reader is referred to Inoué (2016) and Inoué and Kogure (2011).

HAADF-STEM

Two specimens for STEM observations were prepared from the selected areas in petrographic thin sections using a focused ion beam (FIB) apparatus with the micro-sampling system (Hitachi FB-2100). The STEM observations were carried out on two instruments, a JEOL JEM-2800F without a spherical aberration (Cs) corrector and a JEOL ARM-200F with a Cs-corrector for the probe-forming lens. Both instruments were equipped with the Schottky-type field emission electron guns operated at 200 kV. The image resolution expected for the STEM images was 2 Å and 0.8 Å, respectively; the beam convergence semi-angle of the probe was 8.8 mrad and 24 mrad for JEM-2800F and ARM-200F, respectively. The detection semi-angles of the HAADF-detector were between 55 (inner) and 248 (outer) mrad for the JEM-2800F, and between 68 (inner) and 280 (outer) mrad for the ARM-200F. Images taken with the JEM-2800F are referred to as 'Cs-uncorrected' and those taken with the ARM-200F, as 'Cs-corrected' throughout this study. The HAADF images recorded were processed using a Wiener-filter (developed by K. Ishizuka, HRTEM Research Inc.) which was implemented in a Gatan DigitalMicrograph (Kogure & Okunishi, 2010) to remove noise contrast (Marks, 1996; Kilaas, 1998). All images were recorded along one of the X_i ($i = 1$ to 3) directions defined by Bailey (1969) (see Fig. 1a). If the structure is viewed along one of these directions (Fig. 1b), all octahedral sites in the chlorite structure can be recognized as individual spots of 1.5 Å periodicity, particularly in Cs-corrected images.

HAADF-STEM image simulations

Comparison with image simulations for a given structure model is useful to verify the assignment of observed HAADF-STEM images. In the present study, HAADF images were simulated using the FFT

https://doi.org/10.1180/claymin.2016.051.4.05 Published online by Cambridge University Press

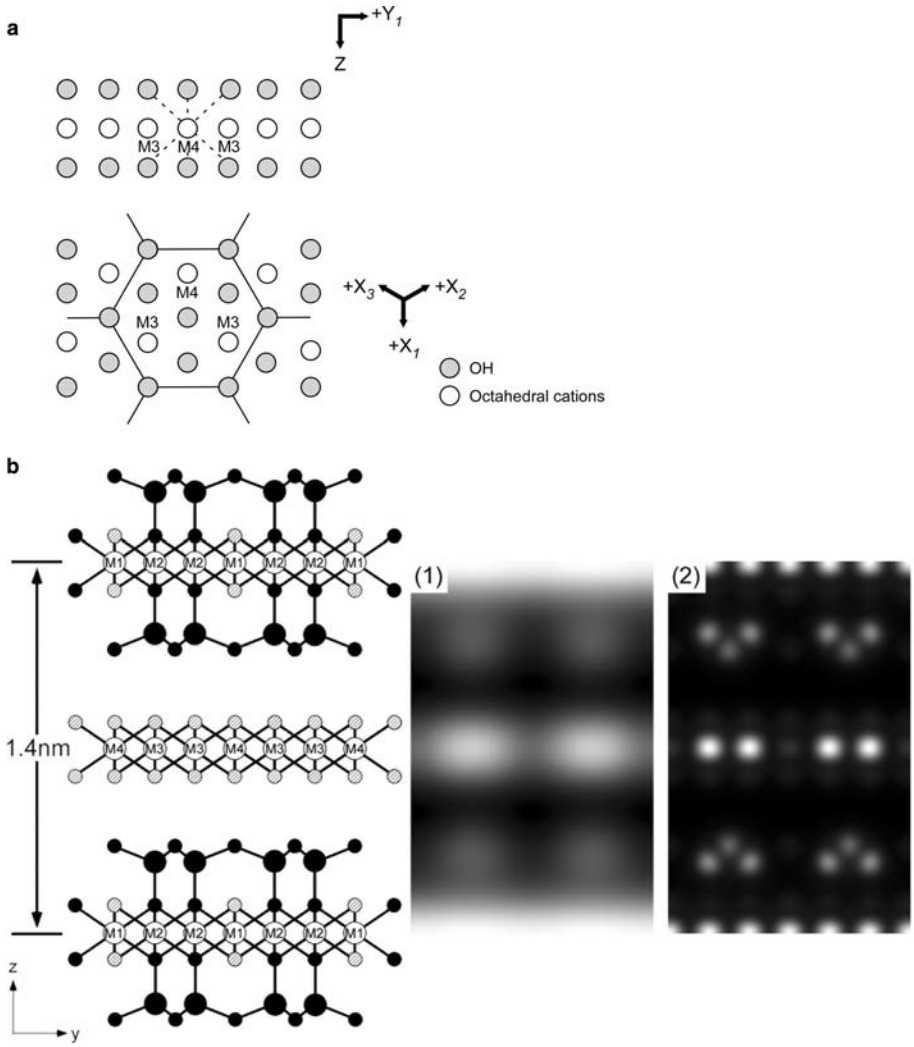

FIG. 1. (a) Schematic diagrams of the B sheet viewed along X and Z directions showing the positions of M3 and M4 sites and X_i directions (i = 1–3). (b) Simulated Cs-uncorrected (1) and Cs-corrected (2) HAADF-STEM images of a hypothetical chlorite ($(Fe_5Al)(Si_3Al)O_{10}(OH)_8$) and the corresponding crystal structure viewed along one of the X_i directions (i = 1–3).

multislice method (xHREM) developed by K. Ishizuka (2002). The structure models of chlorite-I*bb* (Bailey & Brown, 1962) and serpentine of polytype 1*T* (Bailey, 1969) were adopted in the simulations. The values described above were input for the optic and detector parameters of the HAADF-STEM throughout the simulations. The defocus value was set to −3 nm based on the preliminary image simulations (A. Kumamoto, pers. comm.).

RESULTS AND DISCUSSION

HAADF-STEM image simulation of 14 Å chlorite

Figure 1b shows simulated HAADF images of a hypothetical 14 Å Fe-chlorite of $(Fe_5Al)(Si_3Al)O_{10}(OH)_8$ for both Cs-uncorrected and Cs-corrected images, along with the corresponding crystal structure.

https://doi.org/10.1180/claymin.2016.051.4.05 Published online by Cambridge University Press

The simulations assumed a structure model in which octahedral Al preferentially occupied the M4 sites; tetrahedral Si and Al were distributed randomly in the T sites following previous studies (*e.g.* Bailey, 1988a; Welch *et al.*, 1995). The presence of tetrahedral Fe was ignored, taking into account the evidence about Fe distribution in the study sample determined by preliminary Mössbauer spectroscopic measurements (Inoué, unpublished data). Assuming the structure model and chemical composition, the interlayer B sheet with Al and Fe in the M4 and M3 sites was characterized separately by an array of two bright spots and one dark spot, and the octahedral (O-) sheet in TOT exhibited an array of spots with equal brightness because of the identical population of Fe in the M1 and M2 sites. The tetrahedral sheets exhibited a mass of much darker spots between the two octahedral sheets. These features were verified more clearly by the simulations of the Cs-corrected HAADF-STEM image (Figs 1b, 2). Although the simulations of Cs-corrected HAADF images (*e.g.* Figs 1b, 2) highlight the presence of oxygen in the tetrahedral sheets together with the two sites because of the high density in the direction, the presence of the spots was unclear in the actual images of sample.

Figure 2A shows simulated Cs-corrected HAADF-STEM images as a function of sample thickness for two different composition models. Differences in thickness affected not only the brightness of the images but also the contrast ratios between M3 and M4 sites, although the correspondence between contrast and structure model was preserved regardless of specimen thickness (Fig. 2B). The effect of composition is discussed below.

Distribution of octahedral Fe and Al in a 14 Å layer

Figures 3 and 4 show examples of Cs-uncorrected and Cs-corrected HAADF images of 14 Å layers observed in the interstratified minerals after the noise-reduction process. In both images three types of spot arrays were recognized: an array consisted of a set of two bright and one dark spots, a continuous array of spots with nearly identical contrast and that of relatively dark spots, which is similar to the results of simulation on the whole. These features were commonly observed within the specimens studied. Profiles on the lower parts of images correspond to the line profiles of spot-contrast along the a and b lines of Figs 3 and 4. In addition, that on the right-hand side shows a profile of contrasts integrated along the lateral directions of image. Taking into account the results of previous simulations (Figs 1, 2), the three types of spot arrays can be assigned to the interlayer B sheet, the octahedral sheet of the TOT layer and the tetrahedral sheet in the 14 Å layer, respectively. Such assignment was again easier in the Cs-corrected image (Fig. 4). In the B sheet, one dark spot and two bright spots correspond to the M4 and M3 sites, respectively, and the contrast ratio of M4 to M3 sites was 0.38 ± 0.08 on average, measured using a function of a Gatan Digital Micrograph. The bright spots in the O sheet correspond to the M1 and M2 sites, and the contrast ratio of M1 to M2 sites was 0.96 ± 0.04 on average. That of M2 to M3 sites was 0.90 ± 0.01 on average. These contrast ratios imply that the average Z numbers of cations which occupied the M1, M2 and M3 sites are almost equal in the 14 Å layers of sample studied. The integrated contrast of the B sheet along the lateral direction of the image was always darker than that of the O sheet. The contrast ratio of the B sheet to the O sheet was constant at ~0.8, regardless of Cs correction or not (Figs 3, 4).

To elucidate the more detailed distribution of octahedral cations in the B and O sheets, the results of HAADF-STEM observations were compared with image simulations for the actual chemical composition of the sample, assuming various models of cation distribution (Fig. 2). Upon simulation, ferrous and ferric irons were distinguished in order to estimate the numbers of vacancies quantitatively. Inoue *et al.* (2009) and Bourdelle *et al.* (2013) proposed different geothermometers to estimate the temperature of chlorite formation using chemical-composition data. The former method required the data of ferric iron content to be determined independently, whereas the latter did not. Nevertheless, the two methods gave similar estimates of the formation temperature (Bourdelle *et al.* 2013). If this is the case, assuming that the formation temperatures (321°C) estimated by Bourdelle's method are the same as those of Inoue (2009), the $Fe^{3+}/\Sigma Fe$ ratio of the present sample can be estimated, and the result is 0.05. As a consequence, the structure formula of the sample was expressed approximately by $(Fe^{2+}_{4.08}Fe^{3+}_{0.22}Al_{1.5}\square_{0.2})(Si_{2.5}Al_{1.5})O_{10}(OH)_8$. Here the small amounts of Mg and Mn present in the sample were regarded as Al and Fe, respectively, because of the negligible effects on the HAADF-STEM image contrast due to the similarity in the Z numbers.

Previous studies of clinochlore using XRD (*e.g.* Rule & Bailey, 1987; Bailey, 1988a; Zheng & Bailey, 1989), nuclear magnetic resonance (NMR: *e.g.* Welch *et al.*, 1995) and Mössbauer spectroscopy (Smyth

https://doi.org/10.1180/claymin.2016.051.4.05 Published online by Cambridge University Press

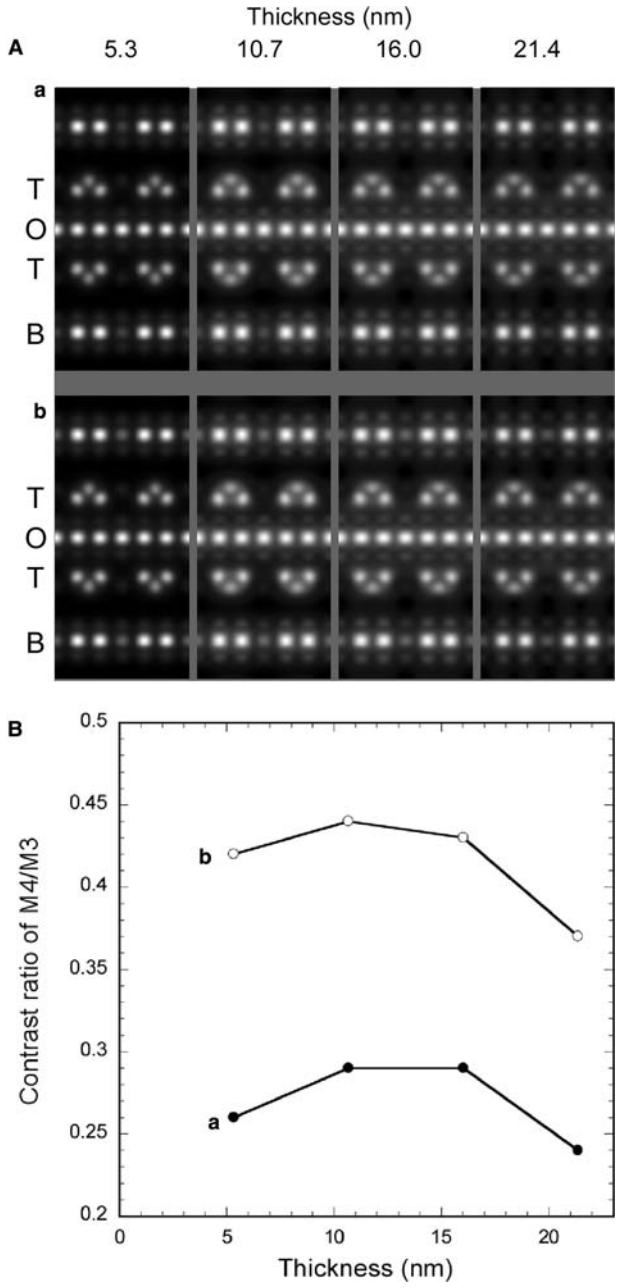

FIG. 2. (A) Simulated Cs-corrected HAADF-STEM images of chlorite with two types of models of octahedral cation distribution (a and b) as a function of sample thickness (see text for the details). (B) The relationships between the contrast ratios of M4 to M3 sites and the sample thickness.

et al., 1997) suggested that octahedral trivalent cations preferentially occupy the M4 site of the B sheet. In addition, calculating the interlayer bonding energy of clinochlore-II*bb* indicated that the preferential occupancy of trivalent cations in the M4 site increased the stability of structure (Bish & Giese, 1981). The

https://doi.org/10.1180/claymin.2016.051.4.05 Published online by Cambridge University Press

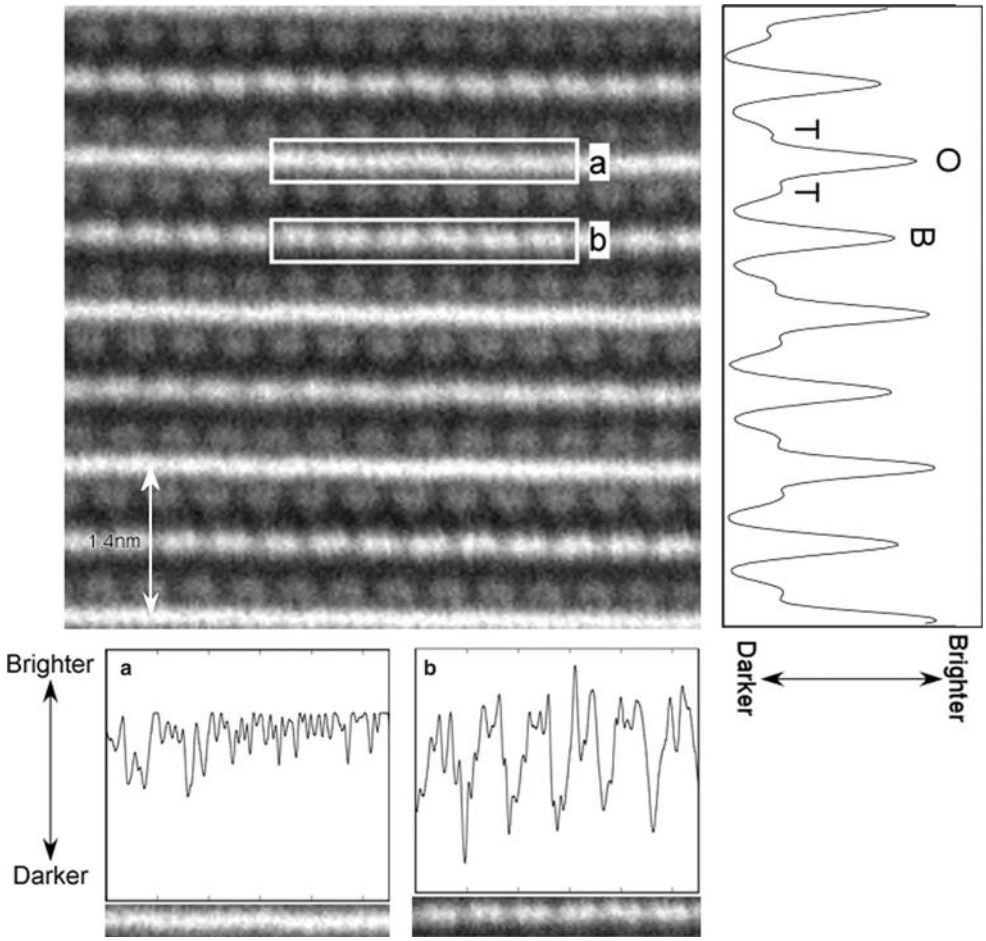

FIG. 3. Cs-uncorrected HAADF-STEM image of 14 Å component layers viewed along one of the X_i directions, the contrast profiles measured from areas in boxes a and b (bottom) and the integral contrast profile of the image perpendicular to the stacking direction (right-hand side). T: tetrahedral sheet, O: the O sheet in the TOT layer, B: the B sheet.

preferential occupancy of the vacancy in the M4 site was not considered in the present study because the effect of the number of vacancies on image simulation was not verified clearly in the preliminary simulations. The following two models were assumed for the distribution of octahedral cations in the O and B sheets of the present Fe-rich chlorite so that the total positive charges in the two models equalize that of the chemical formula mentioned previously:

(a) $(Fe^{2+}_{2.45}Fe^{3+}_{0.13}Al_{0.30}\square_{0.12})_{M1+M2}(Fe^{2+}_{1.63}Fe^{3+}_{0.09}Al_{0.20}\square_{0.08})_{M3}(Al)_{M4}$,

(b) $(Fe^{2+}_{2.45}Al_{0.43}\square_{0.12})_{M1+M2}(Fe^{2+}_{1.63}Al_{0.29}\square_{0.08})_{M3}(Fe^{3+}_{0.22}Al_{0.78})_{M4}$.

Based on the analysis of contrast profiles in the B- and O sheets in Fig. 4 mentioned above, the chemical compositions of the M1, M2 and M3 sites were assumed to be the same. The results of image simulation for the two models are shown in Fig. 2. At first glance, the images for the two models were indistinguishable from each other. However, the contrast ratios in bright spots between the M4 and M3 sites, measured on the simulated Cs-corrected HAADF-STEM images, were varied by the compositions of two sites; the more Fe content there is in the M4 site, the more the contrast ratio of the M4/M3 increases (Fig. 2B). For the 'type a' model, when the Al/Fe ratio of the M4 site is 1.0, the contrast ratio of the M4/M3 sites was much smaller than that in the experimental Cs-corrected images (0.38 ± 0.08) at any specimen thicknesses (Fig. 2B). On the other hand, the

https://doi.org/10.1180/claymin.2016.051.4.05 Published online by Cambridge University Press

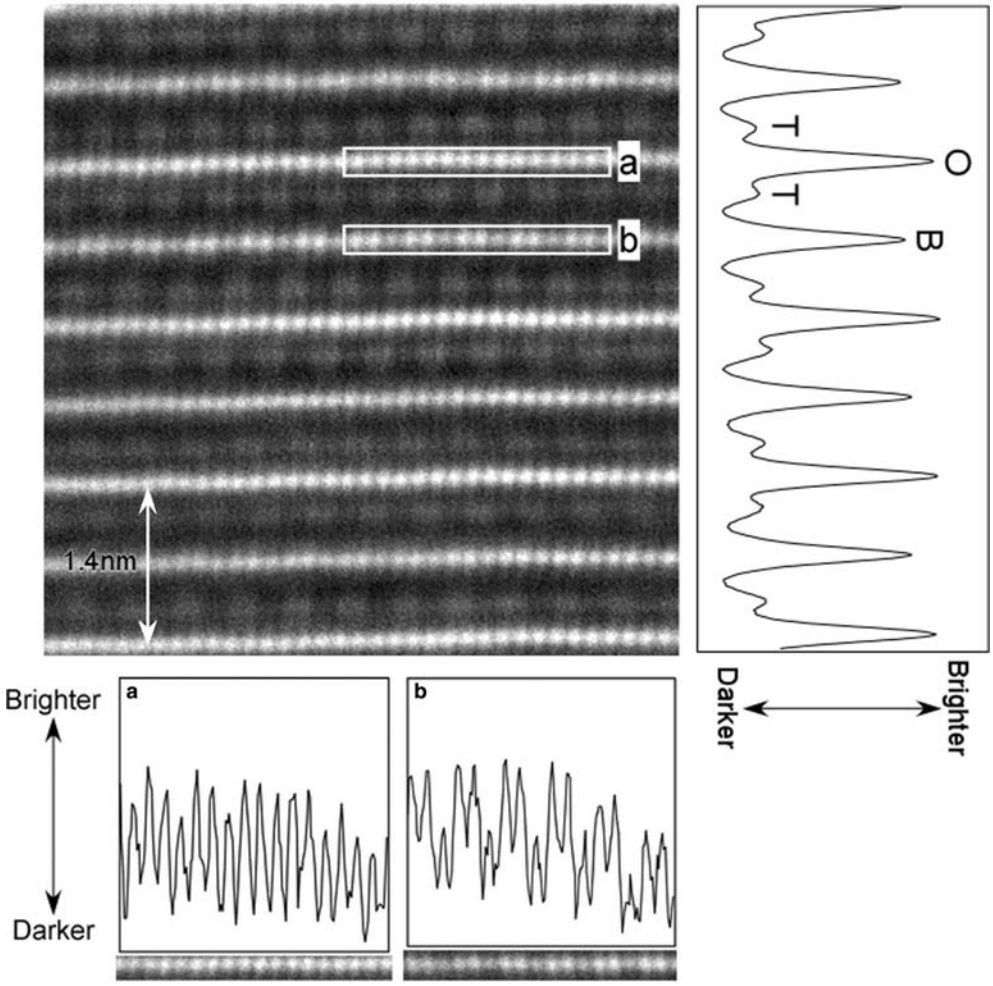

FIG. 4. Cs-corrected HAADF-STEM image of 14 Å layers viewed along one of the X_i directions, and the contrast profiles measured from areas in boxes a and b (bottom) and the integral contrast profile of the image perpendicular to the stacking direction (right-hand side). T: tetrahedral sheet, O: the O sheet in the TOT layer, B: the B sheet.

contrast ratio of the simulated image for the 'type b' model was close to the contrast ratios of M4/M3 sites in the experimental Cs-corrected images at any sample thicknesses. In addition, the integrated contrast ratio of the O and B sheets for the model b was 0.75 at 16.0 nm specimen thickness, which was close to those (0.8) in the experimental images (Figs 3, 4). The slight differences between the simulated and experimental images may be because the actual $Fe^{3+}/\Sigma Fe$ ratio in the studied sample was somewhat larger than the assumed value (0.05). Nevertheless, comparison between the simulated and experimental images suggests that the M4 sites in the B sheet of a 14 Å layer are occupied by Al, associated with a small amount of Fe, probably ferric iron, which is represented approximately by the cation distribution model b. The other sites of M1, M2 and M3 have a similar cation population with an Al/Fe ratio (~0.17), which is quite different from that (~3.5) of the M4 site.

Distribution of octahedral Fe and Al in a 7 Å layer

The samples studied were, in fact, interstratified minerals consisting of the 7 Å and 14 Å component layers. As for the distribution of octahedral cations in

https://doi.org/10.1180/claymin.2016.051.4.05 Published online by Cambridge University Press

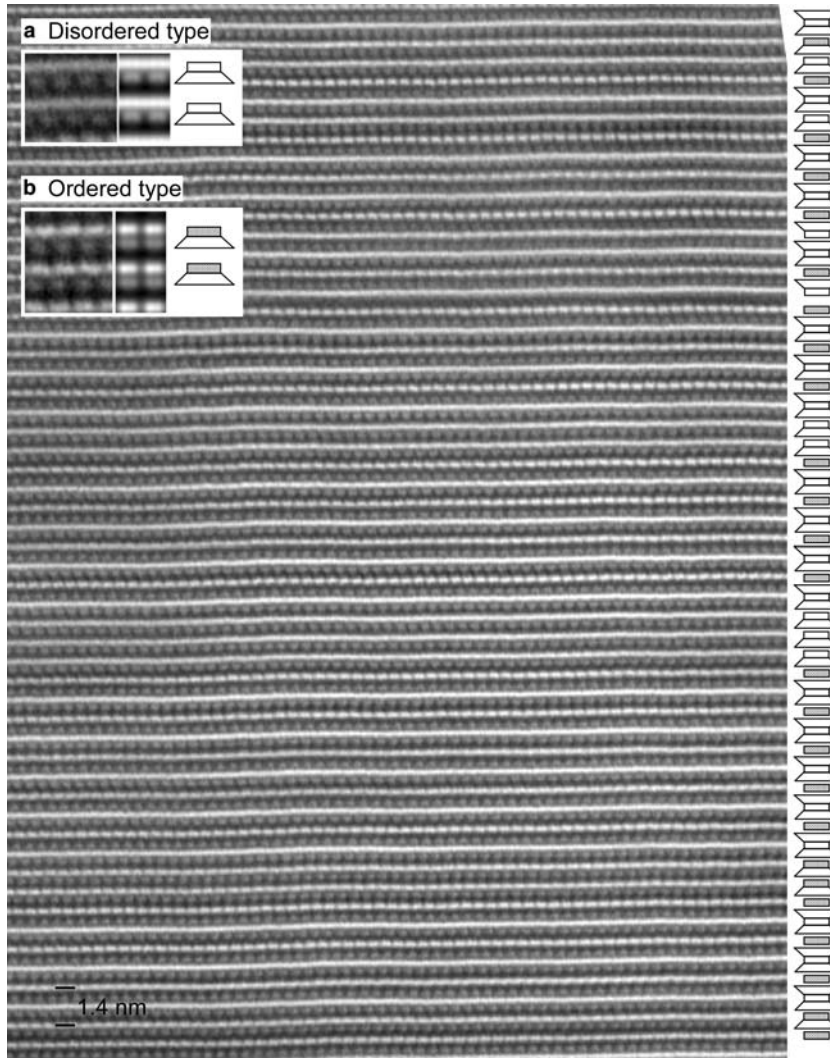

FIG. 5. Cs-uncorrected HAADF-STEM images, together with a schematic diagram showing the stacking sequence (right-hand side). The magnified images of the disordered (a) and ordered (b) types of 7 Å layers are shown in the insets. Trapezoids represent tetrahedral sheets; the white rectangles represent O sheets and disordered-type octahedral sheets in 7 Å layer, and the shaded ones represent the B sheet and ordered-type octahedral sheets in the 7 Å layer.

the 7 Å component layers, two types of 7 Å layers with different octahedral sheets in terms of the contrast were recognized in the Cs-uncorrected HAADF-STEM images (insets in Fig. 5). One type was the 7 Å layer with an octahedral sheet which appeared to be a nearly continuous bright line and the other type was that with an octahedral sheet which appeared to be a bright line with interruptions (insets in Fig. 5). To avoid confusion, here, the 7 Å layer with the former type of octahedral sheet was named the disordered type and that with the latter type of octahedral sheet was named the ordered type. The contrast profiles of the disordered and ordered types of octahedral sheets resembled those of O and B sheets in 14 Å layers mentioned in the previous section, respectively. In the 7 Å layer minerals, three octahedral sites, namely the A, B and C sites, are distinguishable (Bailey, 1969). The HAADF-STEM observations (Fig. 5) indicated that the octahedral cations were distributed randomly in the three sites of the disordered-type 7 Å layers

https://doi.org/10.1180/claymin.2016.051.4.05 Published online by Cambridge University Press

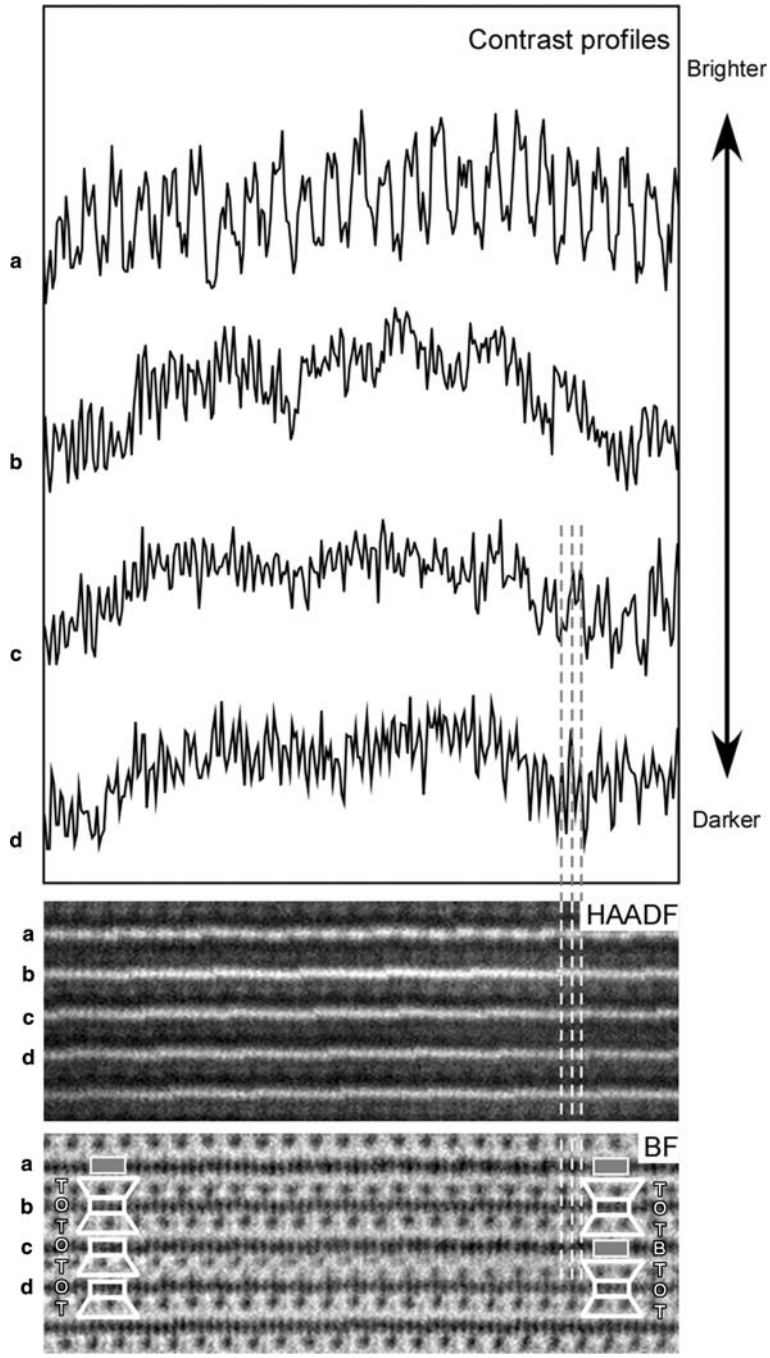

FIG. 6. Magnified Cs-corrected HAADF- and bright field- (BF) STEM images showing the lateral-contact relations of octahedral sheets with different types of cation distribution. Contrast profiles (a–d) were measured along the lines a–d marked in the images. The notched features which appeared in the images were due to artificial noise during image acquisition. (a) B sheet, (b) O sheet, (c) the contact between the disordered octahedral sheet of the 7 Å layer and the B sheet, (d) the contact between the disordered octahedral sheet of the 7 Å layer and the O sheet.

https://doi.org/10.1180/claymin.2016.051.4.05 Published online by Cambridge University Press

because of the array of spots with almost equal contrast, like a line. While an ordered site occupancy of Al occurred in the A sites, it is expected that the ordered-type octahedral sheet exhibits a contrast image similar to the B sheet with M4 sites preferentially occupied by Al in the 14 Å layer.

Vertical and lateral arrangements of 7 Å and 14 Å layers

In the HAADF images shown in Fig. 5, the 14 Å layers gave a regular repetition of TOT-B in a packet locally intercalated by the two types of 7 Å layers defined above. The entire stacking arrangement of 14 Å and two types of 7 Å layers appeared to be random within a packet. More interestingly, the stacking of disordered- and ordered-types of 7 Å layer with opposite polarity was visible locally (Fig. 5), which is a new discovery for the stacking mode in the interstratification of 7 Å and 14 Å layers. Previous studies have reported the interstratified sequence between 14 Å and 7 Å layers with the same polarity (*e.g.* Baronnet, 1997).

Figure 6 highlights the lateral contact relations between the 7 Å and 14 Å layers in the Cs-corrected HAADF images. Two types of lateral contacts in the octahedral sheets of 7 Å and 14 Å layers were distinguishable: one was the contact between the disordered-type octahedral sheet of the 7 Å layer and the B sheet of 14 Å layer (line c in Fig. 6) and the other was that between the disordered-type octahedral sheet and the O sheet of 14 Å layer (line d in Fig. 6). The lateral contact between the ordered-type octahedral sheet and the B sheet was not found in the present study. If the present observations are a general case, taking into account the statistical problem of observation under TEM, the restricted lateral-contact relations between octahedral sheets in 7 Å and 14 Å layers in interstratified structure may reflect the growth process of the mineral in hydrothermal environments. The cause of irregularity may be due to the rapid precipitation of the minerals in hydrothermal environments.

CONCLUSIONS

The HAADF-STEM techniques were applied to extremely Fe-rich interstratified minerals of 7 Å berthierine and 14 Å chlorite. Comparison of observed and simulated images indicated convincingly that Al occupies preferentially the M4 site of the interlayer sheet in Fe-rich 14 Å chlorite. The 7 Å component layer, *e.g.* berthierine, has two types of octahedral sheets, ordered and disordered. Specifically, irregular vertical and lateral contact relations of the component layers were observed within the interstratified structure in the HAADF images. Although the exact cause remains to be resolved, the present study demonstrated not only that HAADF-STEM was able to visualize the distribution of cations in the component layers of fine-grained minerals such as Fe-rich interstratified minerals of 7 Å and 14 Å layers, but also that the new technique provided a clue to understanding the growth mechanism of interstratified minerals at an atomic scale.

ACKNOWLEDGEMENTS

The authors are grateful to Tetsuro Yoneda of Hokkaido University and Atsuyuki Inoue of Chiba University for kindly providing the chlorite samples used in the present study, Akihito Kumamoto and Eita Tochigi of the University of Tokyo for their support and valuable discussions during HAADF-STEM observations, Eiko Fujii for her help with STEM sample preparation using FIB, and Kiyoshi Nomura of the University of Tokyo for his help with Mössbauer analysis. The authors thank Huifang Xu, Fernando Nieto and an anonymous reviewer for their valuable and constructive comments which helped to improve an early version of the manuscript. Some of this work was supported by the 'Nanotechnology Platform' (project No.12024046) of the Ministry of Education, Culture, Sports, Science and Technology (MEXT), Japan. S.I. was supported by a Research Fellowship of the Japan Society for the Promotion of Science (JSPS).

REFERENCES

Ahn J.H. & Peacor D.R. (1985) Transmission electron microscopic study of diagenetic chlorite in Gulf Coast argillaceous sediments. *Clays and Clay Minerals*, **33**, 228–236.

Bailey S.W. (1969) Polytypism of trioctahedral 1:1 layer silicates. *Clays and Clay Minerals*, **17**, 355–371.

Bailey S.W. (1988a) Chlorites: structures and crystal chemistry. pp. 347–403 in: *Hydrous Phyllosilicates (Exclusive of Micas)* (S.W. Bailey, editor). Vol. **19**, Reviews in Mineralogy, Mineralogical Society of America, Washington, D.C.

Bailey S.W. (1988b) Structures and compositions of other trioctahedral 1:1 phyllosilicates. Pp. 169–188 in: *Hydrous Phyllosilicates (Exclusive of Micas)* (S.W. Bailey, editor). Vol. **19**, Reviews in Mineralogy, Mineralogical Society of America, Washington, D.C.

Bailey S.W. & Brown G. (1962) Chlorite polytypism: I. regular and semirandom one-layer structures. *American Mineralogist*, **47**, 819–850.

Baronnet A. (1997) Equilibrium and kinetic processes for polytypes and polysome generation. Pp. 119–152 in:

https://doi.org/10.1180/claymin.2016.051.4.05 Published online by Cambridge University Press

Modular Aspects of Minerals (S. Merlino, editor). Vol. **1**, EMU Notes in Mineralogy, Eötvös University Press, Budapest.

Bish D.L. & Giese R. (1981) Interlayer bonding in IIb chlorite. *American Mineralogist*, **66**, 1216–1220.

Bourdelle F., Parra T., Chopin C. & Beyssac O. (2013) A new chlorite geothermometer for diagenetic to low-grade metamorphic conditions. *Contributions to Mineralogy and Petrology*, **165**, 723–735.

Hillier S. (1994) Pore-Lining Chlorites in siliciclastic reservoir sandstones: electron-microprobe, SEM and XRD data, and implications for their origin. *Clay Minerals*, **29**, 665–679.

Inoué S. (2016) *Study of Fe-rich chlorite and 7Å-14 Å interstratified minerals using high-resolution electron microscopy.* PhD Thesis, the University of Tokyo, Japan, 132 pp.

Inoué S. & Kogure T. (2016) High-resolution transmission electron microscopy (HRTEM) study of stacking irregularity in Fe-rich chlorite from selected hydrothermal are deposits. *Clays and Clay Minerals*, **64**, 131–144.

Inoue A., Meunier A., Patrier-Mas P., Rigault C., Beaufort D. & Vieillard P. (2009) Application of chemical geothermometry to low-temperature trioctahedral chlorites. *Clays and Clay Minerals*, **57**, 371–382.

Ishizuka K. (2002) A practical approach for STEM image simulation based on the FFT multislice method. *Ultramicroscopy*, **90**, 71–83.

Jiang W.T., Peacor D.R. & Slack J.F. (1992) Microstructures, mixed layering, and polymorphism of chlorite and retrograde berthierine in the Kidd Creek massive sulfide deposit, Ontario. *Clays and Clay Minerals*, **40**, 501–514.

Kilaas R. (1998) Optimal and near-optimal filters in high-resolution electron microscopy. *Journal of Microscopy*, **190**, 45–51.

Kogure T. & Drits V.A. (2010) Structural changes in celadonite and cis-vacant illite by electron radiation in TEM. *Clays and Clay Minerals*, **58**, 522–531.

Kogure T. & Okunishi E. (2010) Cs-corrected HAADF-STEM imaging of silicate minerals. *Journal of Electron Microscopy*, **59**, 263–271.

Marks L.D. (1996) Wiener-filter enhancement of noisy HREM images. *Ultramicroscopy*, **62**, 43–52.

Pennycook S.J. & Jesson D.E. (1992) Atomic resolution Z-contrast imaging of interfaces. *Acta Metallurgica et Materialia*, **40**, S149–S159.

Rule A.C. & Bailey S. (1987) Refinement of the crystal structure of a monoclinic ferroan clinochlore. *Clays and Clay Minerals*, **35**, 129–138.

Shikazono N. (2003) *Geochemical and Tectonic Evolution of Arc-Backarc Hydrothermal Systems: Implication for the Origin of Kuroko and Epithermal Vein-Type Mineralizations and the Global Geochemical Cycle.* Elsevier, Amsterdam, 463 pp.

Slack J.F., Jiang W.T., Peacor D.R. & Okita P.M. (1992) Hydrothermal and metamorphic berthierine from the Kidd Creek volcanogenic massive sulfide deposit, Timmins, Ontario. *The Canadian Mineralogist*, **30**, 1127–1142.

Smyth J.R., Dyar M.D., May H.M., Bricker O.P. & Acker J.G. (1997) Crystal structure refinement and Mössbauer spectroscopy of an ordered, triclinic clinochlore. *Clays and Clay Minerals*, **45**, 544–550.

Welch M.D., Barras J. & Klinowski J. (1995) A multinuclear NMR study of clinochlore. *American Mineralogist*, **80**, 441–447.

Wicks F. & O'Hanley D.S. (1988) Serpentine minerals; structures and petrology. Pp. 91–167 in: *Hydrous Phyllosilicates (Exclusive of Micas)* (S.W. Bailey, editor). Vol. **19**, Reviews in Mineralogy, Mineralogical Society of America, Washington D.C.

Xu H.F. & Veblen D.R. (1996) Interstratification and other reaction microstructures in the chlorite-berthierine series. *Contributions to Mineralogy and Petrology*, **124**, 291–301.

Xu H., Shen Z., Konishi H. & Luo G. (2014) Crystal structure of Guinier-Preston zones in orthopyroxene: Z-contrast imaging and *ab inito* study. *American Mineralogist*, **99**, 2043–2048.

Zheng H. & Bailey S.W. (1989) Structures of intergrown triclinic and monoclinic IIb chlorites from Kenya. *Clays and Clay Minerals*, **37**, 308–316.

https://doi.org/10.1180/claymin.2016.051.4.05 Published online by Cambridge University Press